Dynamic strain propagation in nanoparticulate zirconia refractory

Jones, Morgan; Fearn, Stephen; Winter, Rudolf; Yuan, F.; Lennie, A. R. ; Parker, J. E.; Thompson, S. P.; Tang, C. C.

Published in:
Journal of Applied Crystallography

DOI:
10.1107/S1600576715002393

Publication date:
2015

Citation for published version (APA):
Jones, M., Fearn, S., Winter, R., Yuan, F., Lennie, A. R., Parker, J. E., ... Tang, C. C. (2015). Dynamic strain propagation in nanoparticulate zirconia refractory. Journal of Applied Crystallography, 48, 386-392. https://doi.org/10.1107/S1600576715002393

Dynamic strain propagation in nano-particulate zirconia refractory

Morgan E Jones,[a]* Steve Fearn,[a] Rudolf Winter,[a] Fajin Yuan,[b] Alistair R Lennie,[b] Julia E Parker,[b] Stephen P Thompson[b] and Chiu C Tang[b]

[a]*Department of Physics, Physical Sciences Building, Aberystwyth University, Aberystwyth, SY23 3BZ Wales, and* [b]*Beamline I11, Diamond Light Source, Harwell Campus, Didcot, OX11 0DE England. E-mail: mgj7@aber.ac.uk*

Laser; In-situ; X-ray Powder Diffraction; Zirconia; Dynamic Strain; Microstrain; Structural Refinement; Whole Powder Pattern Fitting

Abstract

Residual and intrinsic strains in granular materials have been studied extensively. However, understanding the dynamic strains which cause these resultant residual strains is key to developing better strain resistant materials. This investigation demonstrates a method for characterising dynamic strain propagation in granular materials. The specimen is a zirconia based refractory composed of sol-gel derived zirconia nanoparticles in a potassium-silicate glass binder. *In-situ* synchrotron X-ray powder diffraction in flat-plate geometry is used to characterise sample structure on the order of 1 ms. A 125 W CO_2 laser is used to strain the sample with a 25 ms pulse length. Due to poor flux on this time-scale a pump-probe method is repeated 1000 times and subsequently re-binned to improve statistics. A Gaussian weighting function is

also used to introduce better contrast between strained and unstrained frames. Topas Academic is used for fitting with a le-Bail model in 'batch mode'. Lattice parameters and sample height are refined during fitting, along with a Lorentzian line-width for extracting microstrain broadening. Microstrains, ε, in the range of $1.01\% < \varepsilon < 1.46\%$ are reported on a 1 ms time-scale.

1. Introduction

Many materials applications require compounds that can withstand rapid thermal cycles, ranging from Solid Oxide Fuel Cells (SOFC's) to furnace refractories (Matus *et al.*, 2005; Steele & Heinzel, 2001; Chou & Stevenson, 2002; Hsiao & Selman, 1997). Operating temperatures for SOFC's range from $973-1273$ K (Ivers-Tiffée *et al.*, 2001), however, complications occur when these materials must also withstand rapid thermal cycling from $573-1073$ K within a few seconds (Bujalski *et al.*, 2007). Thermal barrier coatings for combustion engines also experience similar rapid thermal cycling processes. The key to developing these materials requires an in-depth understanding of the dynamics of the systems. Experimental studies have been published involving residual stresses of thermally cycled zirconia based barrier coatings (Teixeira *et al.*, 1999) but understanding the dynamic processes causing these residual stresses will allow for better design of these kinds of materials.

When a material experiences rapid temperature changes as described above, there are two effects taking place. The first is thermal expansion, propagating radially from the strain source. The second effect is a thermo-kinetic effect which propagates in the form of an acoustic wave throughout the material. Due to the anisotropic nature of crystal structures the acoustic waves propagate along the most energetically beneficial lattice plane within the material (Musgrave, 1970). However, since the material in question is polycrystalline, this is only true within a single grain. In a polycrystalline

medium the acoustic wave propagates along preferred lattice planes towards a grain contact point. The acoustic wave crosses the grain boundary into the neighbouring grain, causing strain. In this example the material is assumed to consist of hard grains with a grain boundary of negligible thickness, which means the strain wave propagates between grains undamped. As the strain propagates between grains each subsequent transmission of strain produces a secondary strain source, the magnitude of which depends on the cross-sectional area of the grain contact. Once the strain has crossed the grain boundary, the propagation continues along the new preferred lattice plane continuing on to the next grain boundary (Figure 1).

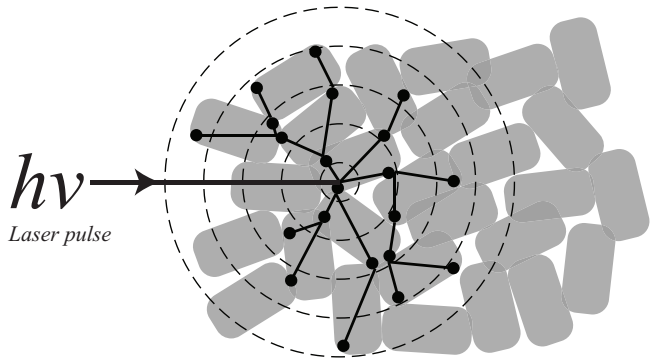

Fig. 1. Strain propagation in granular materials: two propagation mechanisms are in effect. The dotted line demonstrates thermal expansion propagating radially throughout the bulk of the sample while the solid black lines show the propagation of the strain wave along the energetically beneficial lattice planes. The small black nodes show the points of strain transfer between grains.

In-situ studies have been performed on single crystal materials which attempt to follow pico-second acoustic wave propagations both on the surface and in the bulk (Rose-Petruck *et al.*, 1999; Reis *et al.*, 2001; Lee *et al.*, 2005). However, barrier coatings and SOFC's are polycrystalline in nature and therefore an experimental technique is needed which is able to characterise these effects in a polycrystalline medium. The material considered in this study is a zirconia based furnace refractory. Furnace refractories undergo thermal cycling where temperature changes occur on a timescale of the

order of seconds. At this point it is crucial to note that it is not the absolute change in temperature within a time-frame that is important, but the rate of temperature change, since it is this rate of change that creates the wave front of strain. The laser technique subjects the sample to faster temperature changes in order to perform an aggravated test. Since the material in this study is of a granular nature, the time-scale for the propagation of these waves is very different to the single crystal experiments described above. Therefore this study proposes an in-situ method for following strain propagation in granular ceramics on the order of a millisecond while providing an adequate powder average. In-situ synchrotron x-ray powder diffraction (SXPD) is the ideal technique for this task (Cheetham & Goodwin, 2014).

2. Experimental Procedure

2.1. Sample Preparation

The sample used in this investigation consists of sol-gel derived monoclinic zirconia nanoparticles suspended in a potassium silicate glass binder (Le Messurier *et al.*, 2006). Nanocrystalline zirconia particles were produced using zirconium tetrachloride mixed with ammonium hydroxide, NH_4OH to form a gel (Prabhu & Bourell, 1995; Theunissen *et al.*, 1989). The gel was then washed and dried several times to remove the chlorine; this process produced a powder. The powder was then dried at 373 K. This temperature removes excess water whilst being cool enough to avoid calcination.

The potassium silicate binder was produced using 0.3 mol quartz, SiO_2, with 0.1 mol potassium carbonate, K_2CO_3. The mixture was then heated to 1573 K for 2 hrs, then 1623 K for 0.5 hrs and finally at 1673 K for 0.5 hrs. This heating strategy was employed to ensure a homogeneous glass melt. This hot mixture was not quenched, but allowed to cool in air followed by ball-milling to produce a fine glass powder.

The refractory sample was formed by thoroughly mixing 90 wt% zirconia nano-

particles with 10 wt% potassium-silicate glass powder and then pressed to form a 13 mm diameter, 400 μm thick pellet using a force of 10 t. These pellets were then sintered at 1000 K for 1 hr in order to collapse pores and form a continuous glass matrix. The sintering was performed in alumina crucibles which have contributed a minor alumina phase to the samples.

2.2. Experimental Setup

In-situ SXPD was conducted at beamline I11 at the Diamond Light Source (Thompson *et al.*, 2009). The Mythen position sensitive detector (PSD) at I11 collects 120° 2θ simultaneously at very short frame sizes down to 1 ms (Thompson *et al.*, 2011). X-ray spot size was carefully considered to ensure good powder averaging whilst minimising the amount of unstrained material within the incident beam. Incident X-ray photons had a calibrated energy of 12 keV. The X-ray beam size was 1.5 mm in the horizontal and 0.1 mm in the vertical direction.

Figure 2(a) shows the sample environment developed to house the sample and enclose the laser radiation. The environment is fixed to the laser via a beam tube. The laser used in this experiment was a Synrad 125 W CO_2 laser ($\lambda = 10.59\mu m$). The beam has a Gaussian beam profile and a beam diameter of 1 mm (fwhm). The laser radiation was incident normal to the sample surface and the X-ray radiation was incident at 9°θ to the sample surface. An Al coated Mylar window protected the detector from any stray IR radiation whilst not affecting the powder diffraction. Considering that the rise time of the laser is 150 μs, the data acquisition starts at the beginning of this rising flank in order to ensure observation of strain (figure 2(b)). At 95% power and a shot length of 25 ms the laser outputs 2.96 J into the sample. However, since the data acquisition occurs during the first 1 ms of the laser pulse, the energy supplied to the sample during the x-ray exposure is considered to be 0.12 J.

It is important to consider the heating caused by this laser power. If all of the energy output by the laser were heat, and all of this heat were absorbed by the sample (which is an overestimation), the temperature change exhibited by the sample within the 1 ms time frame of a single exposure would be given by equation 1:

$$\Delta T = \frac{Q}{mC} \tag{1}$$

where Q is the heat added, m is the mass at the strain source region and C is the specific heat of zirconia ($0.502\ Jg^{-1}K^{-1}$) (Pouchon *et al.*, 1998). For the beam dimensions in this experiment, the maximum temperature change in the strain source region after 1 ms of heating is therefore 27 K. Due to limitations of the laser control, the laser irradiation continues for 24 ms beyond the end of the X-ray exposure, increasing the temperature at the strain source by at most a further 648 K based on the same assumptions. A duty cycle of 2 s is used to ensure that this heat is effectively dissipated. The heat is dissipated into the much larger bulk of the sample (about 500 times the mass of the strain source) and the aluminium heat sink to which the sample is mounted.

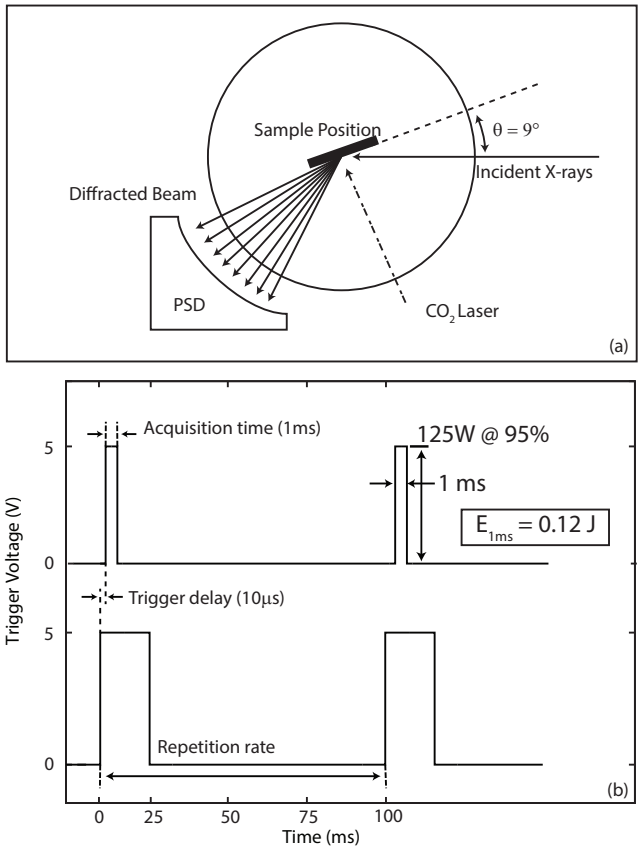

Fig. 2. (a) Geometry of the experiment. X-rays are incident at 9° to the surface, laser light is incident to the normal (b) - Pulse diagram for the firing sequence of the laser and Mythen detector; an SRS DG535 delay generator was used to deliver both signals. The calculation for laser output at 1 ms is also shown in figure (b).

The laser is used as a strain source and the X-rays characterise the sample's response to the incident laser radiation. The displacement between the impact site (laser beam position) and X-ray spot (for characterisation) is varied in order to achieve a spatial representation of the sample's response. The laser beam position is fixed on the sample surface, while the position of the X-ray beam is varied. The displacement of the X-ray spot relative to the laser spot is achieved by moving the whole sample environment normal to the plane spanned by the X-ray and laser beams (out of plane of figure 2(a)). The displacement was varied in 1 mm steps from 0 mm (pump and probe in the same location) to 7 mm displacement. The 0 mm displacement is at the point where

the beam centres coincide, i.e. the displacement is measured as the distance between the centre of both beams.

Both data acquisition and firing of the laser were controlled using an SRS DG535 signal generator. This allows for high temporal resolution when controlling the pump-probe sequence with a jitter of less than 100 ps. A schematic of the firing sequence is shown in figure 2(b). The PSD is a 1D detector covering high 2θ (covering up to 9°) with an angular resolution of 0.004° and frame rate of up to 1 kHz and as such is well suited to the application. However, since the detector is only 8 mm wide out of plane (γ direction), the count rates of a single 1 ms frame are quite low, even with the high flux of the Diamond synchrotron. Therefore, the experiment is repeated at least 1000 times in order to improve diffraction statistics. See figure 3 for a comparison of a single 1 s exposure and 1000 $\times$ 1 ms summed exposures.

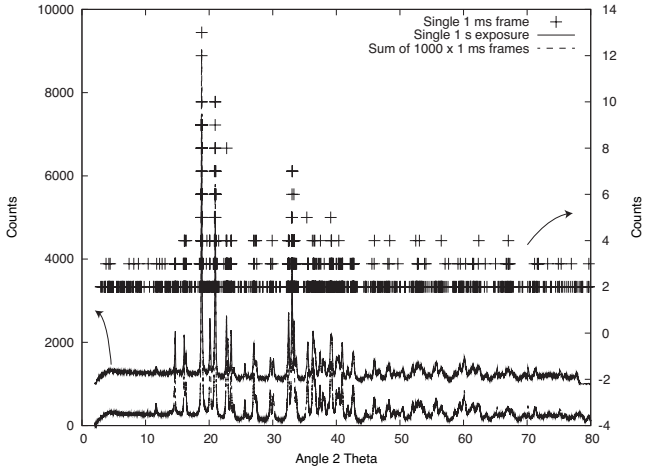

Fig. 3. shows reference scans taken without laser irradiation which demonstrate that the signal-noise ratio of 1000 summed 1 ms frames is comparable to that of a single, conventional 1 s exposure. The figure also shows the count rates achievable in a single 1 ms frame. While the strongest Bragg peaks are clearly visible, it is clear that line profile analysis requires summing multiple exposures to achieve sufficiently good statistics.

Another consideration when conducting this experiment is the propagation velocity of the strain wave. The typical acoustic wave velocity in a polycrystalline ceramic is of

the order of 10^3 m/s (Salamatov, 2007) but varies depending on the material composition and its properties, e.g. microstructure, domain size, porosity and temperature. Since the acoustic wave passes through the material at high velocity, the probability of strained material being in the beam is quite small. Therefore only some frames will contain dynamic strain information.

3. Results and Discussion

Topas Academic (Coelho, 2004) is used to perform all non-linear least squares refinement of the SXPD Data. A le-Bail model (Le Bail, 2005) is used along with the Fundamental Parameter method; this model is used since we cannot rule out that texture may affect the relative intensities of different Bragg peaks. The domain size of the refined phases is fixed at 130 nm for alumina and 80 nm for monoclinic zirconia based on the refinement prior to the first laser shot and supported by SEM (see supplementary information). No significant change in domain size is expected since the sample temperature away from the laser impact site isn't high enough for particle growth of zirconia (for comparison, the melting point of zirconia is 2949 K) (Ronchi & Sheindlin, 2002). The values for domain size are determined by refining Lorentzian domain size parameters when fitting reference scans of the sample and are supported by SEM (see supplementary information). The microstrain broadening for the sample is refined using the Lorentzian strain parameter within Topas. Due to the low signal to noise ratio of the powder patterns, the refinement was moving between several minima. In order to avoid this behaviour, the number of fit parameters was reduced by fixing a Gaussian strain parameter to a constant value of 0.1. This value was determined by performing fits with varying combinations of Lorentzian and Gaussian strain broadening values, and choosing the combination which produced the most stable fit over all displacements. The FWHM of the line width is used to calculate a microstrain

fit parameter, a,

$$Lor_{FWHM} = a \tan\theta \tag{2}$$

as explained in (Balzar, 1999). It is evident from figure 3 that a single 1 ms exposure is not enough to determine any structural details of the sample. Therefore by performing a rolling average of the 1 ms frames it is possible to obtain an increased time resolution which allows for successful Whole Powder Pattern Fitting (WPPF) of the powder diffraction patterns.

3.1. Analysis of averaged data

Initially, each group of 1000 frames was summed to form diffraction patterns representative of the whole data set. These diffraction patterns are then fitted using Topas Academic to extract macrostrain information. A goodness of fit (gof) in the range of 1.4 was achieved with an R_{wp} of 6.1, which considering the small diffraction intensity, is acceptable. The macrostrain, ε, in a particular crystallographic orientation is the variation of the lattice spacing in that direction,

$$\varepsilon = \frac{\Delta d}{d_0}. \tag{3}$$

Figure 4 shows the calculated macrostrain in the direction of each lattice vector for the zirconia phase, plotted against the displacement from the shock site. It is noted that the peak intensity of strain is not at the shock site but rather near 1 mm displacement. This evidence suggests that this is not a thermal effect since peak strain due to thermal expansion would always be at the heat source. In order to produce a macrostrain of 0.003 Å ($\delta d = 0.12$ Å), a temperature increase by 1500 K would be needed at a time of 1 ms. For the temperature change calculated in section 2, a macrostrain of 0.0002 Å would be induced in the sample and is shown as the dashed line in figure 4.

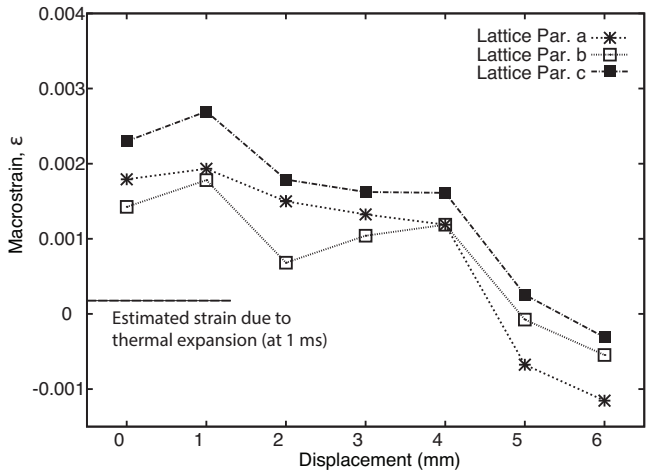

Fig. 4. Macrostrain vs pump-probe displacement (away from the laser spot) in *mm*. The error bars are not shown since they are smaller than the symbol (10^{-5}Å). The dotted line shows the expected thermal expansion to be seen at 1 ms at a temperature change of 27 K.

3.2. Pushing the limits of time resolution

Since a single 1 ms frame (the raw diffraction data collected during the experiment) contains no usable data in its current state, multiple frames were combined into *bins* in order to achieve acceptable data quality. Rolling averages of N consecutive frames (individual exposures following a laser impact) were summed into bins such that the i^{th} bin contains the sum of the frames numbered $(i - N/2)$ to $(i + N/2)$. This process was repeated for different bin sizes, N, ranging from 70 to 250 frames. Two binning methods were used and compared in order to find the most suited. Figure 5(a) describes the two binning methods. One method is an unweighted sum, while the other is a Gaussian weighted sum. The unweighted binning method provides no insight into which of the containing frames is contributing the strain information. However, the Gaussian weighting increases the contrast between the central frame and neighbouring frames within the bins. This contrast focuses on the central frame of each bin which allows for distinction between the strained 1 ms frames and the neighbouring unstrained frames,

while the unstrained frames improve background statistics.

Figure 5(b) shows the comparison of the two binning methods. The c lattice parameter of the monoclinic zirconia phase is plotted (as an example) against bin number, showing the progression of the lattice parameter with respect to number of shots. Lattice parameters a and b exhibit a similar oscillatory nature. While the bin number axis is not a direct representation of elapsed time, it does show the cumulative effects of successive laser pulses in chronological order. It is clearly shown that there is a contrast in signal to noise with the two summing methods. The unweighted data is quite noisy but some features are visible nonetheless. In contrast, the Gaussian weighting produces data that has very little noise but has clearly visible features that change with respect to the number of shots. With this evidence, the Gaussian weighted binning regime was chosen for the remainder of the study.

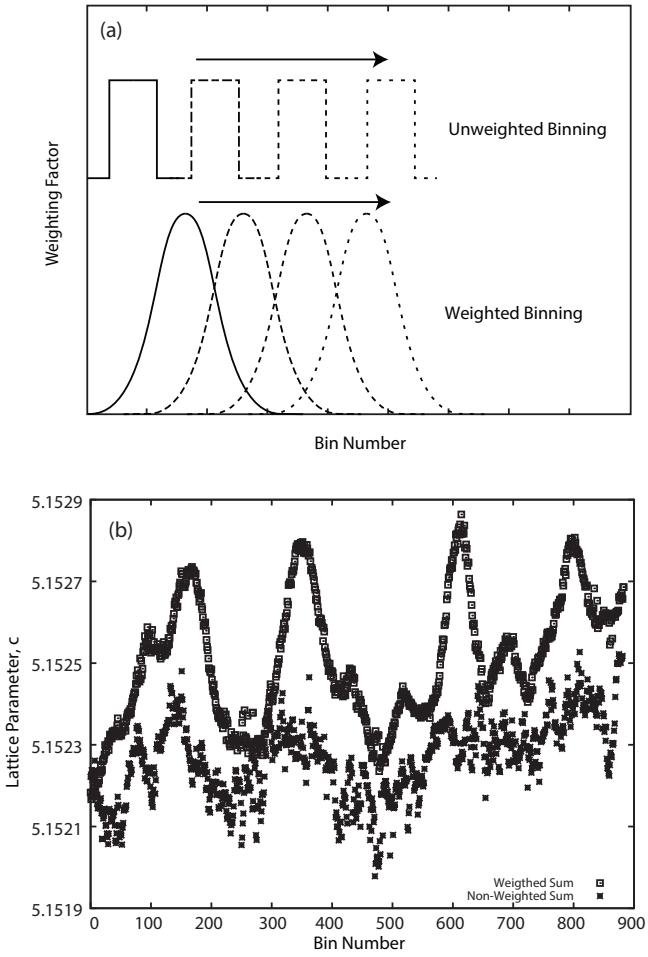

Fig. 5. (a) Unweighted vs Gaussian weighted binning of the data. The weighting factor represents the weighting of each frame relative to its neighbouring frames, (b) Lattice parameter c vs bin number. The plot is a comparison of the lattice parameter c for the re-binned data, both unweighted and Gaussian weighted.

The bins were then fitted with the same model as the total summed diffraction patterns. These groups of bins were fitted in a batch mode, where each bin was fitted with the same initial parameter values derived from the previous analysis of averaged data (sec 3.1). Lattice parameters, sample height and Lorentzian strain were refined in these models. The gof values for these various fits was in the range of $2.1 < gof < 2.5$ and an R_{wp} of 7.8. Figure 6 is an example of the fit for the 81 ms bin size.

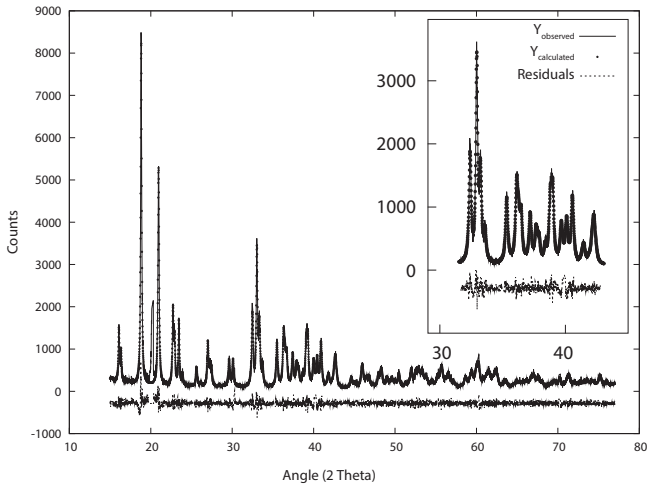

Fig. 6. An example of one of the 81 ms frames and the corresponding fit with residuals. The inset is one portion of the fit magnified.

These parameters are expected to evolve during the shocking. Since the thermal load away from the immediate laser impact is small, the particles are not expected to grow. Due to this and the strong correlation of the domain size and strain fit parameters, the domain size is fixed during refinement.

With decreasing bin size the quality of the diffraction patterns diminishes in two ways: The signal to noise ratio diminishes, and the stability of the fitting is compromised. However, as the bin size increases, the ratio between strained and unstrained frames decreases, averaging information from strained and unstrained parts of the sample. This means that, in order to achieve the optimum results, the smallest possible bin size is needed which does not prohibitively compromise the quality of the fit. The optimum bin size was found to be 81 frames, and is the bin size used for all bin number plots. This was determined by fitting many different bin sizes in order to achieve a balance between the diminishing signal to noise ratio and the averaging out of strain information. Figure 7 shows the Lorentzian strain fit parameter plotted against bin number. The data exhibits an oscillatory nature as the number of shocks increases. This suggests that there is a periodic build-up and subsequent release of

strain within the sample.

In order to understand the data, the Lorentzian strain broadening fit parameter (here-in referred to as microstrain) and the lattice parameters of the monoclinic unit cell are monitored. The evolution of these parameters is plotted in figures 7 and 5(b) with increasing number of shots. Both macrostrain and microstrain oscillate with increasing number of shocks. The amplitude of the strain oscillation peaks increases with number of shocks also. In order to obtain a value for the strain experienced by the sample on a 1 ms time scale, amplitudes of the most intense peaks of each microstrain profile are evaluated for various bin sizes.

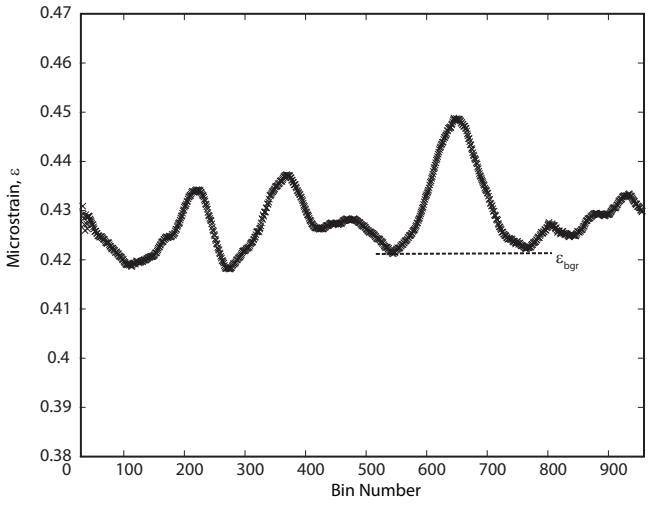

Fig. 7. Evolution of microstrain parameter with respect to bin number. Oscillation can be seen in the microstrain suggesting a mechanism for build up and release of strain within the sample.

The microstrain amplitude is the height of the strongest strain oscillation peak with respect to the background, where the background is the strain in the sample once the material has completed the strain oscillation. The background is determined by fitting a cubic spline to the oscillating curve, with nodes placed at every local minimum in the oscillating plot. The amplitude is then calculated as the difference between the maximum and corresponding minimum.

The oscillatory nature of the strain curve also serves as evidence that the domain size is not changing dramatically. If the domain size were to be subjected to a large change, resulting in a severe broadening of the diffraction pattern, the change could be miss-interpreted for strain-broadening. However, due to the oscillatory nature of the strain curve (i.e. the strain curve returns to a background value post-oscillation) the domains are not fracturing, since this would cause a permanent increase in the FWHM of the line profile, not a transient broadening as seen in the strain oscillation curves.

Figure 8 shows microstrain amplitude plotted against bin size. The plot shows an increase in strain as the bin size decreases. This is to be expected due to an increase in the ratio between strained and unstrained frames within a bin. Considering the decreasing bin size, it is possible to build a simple numerical model to fit the data, allowing us to extract a value for the strain within a single 1 ms frame, as opposed to a strain averaged over a bin size of N frames.

To begin, we assume that one frame within a particular bin contains more strain than its *neighbouring* frames because of the transient additional component due to the strain wave caused by the impact. We define a bin, which contains one strained frame and $(N-1)$ unstrained frames. The strained frame contains a strain of ε_1 and the unstrained frames contain only a much lower background strain of ε_0, while assuming all unstrained frames are equal. Background strain is the term used to describe the residual strain after N shots. Since each shot induces some small residual strain within the sample, the background strain is the accumulated residual strain from all preceding shots to the sample. It is then possible to summarise the strain for a particular bin of size N as

$$\varepsilon(N) = \frac{\varepsilon_1 + (N-1)\varepsilon_0}{N} \tag{4}$$

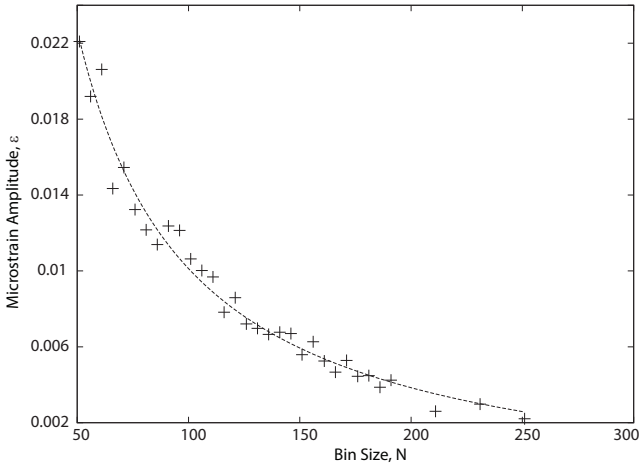

Fig. 8. Lorentzian strain amplitude, ε, vs bin size, N. The dashed line represents a fit based on equation 4.

where N is the total number of frames in the bin. This method allows the extraction of the strain information for one strained frame without measuring the strain directly, which is impossible for a polycrystalline material on this time-scale due to the need for powder averaging. Since ε_1 is a value for the microstrain amplitude, the absolute strain parameter value is $\varepsilon_1 + \varepsilon_{bgr}$, where ε_{bgr} is the background strain from figure 7. As explained in (Balzar, 1999) the true value for the microstrain within a sample, $\Delta d/d$, is shown to be

$$\frac{\Delta d}{d} = \frac{a * \pi}{360}, \tag{5}$$

where a is the Lorentzian strain parameter from fitting. The resulting microstrains at various displacements are in the range $1.01 < \varepsilon < 1.46$. These microstrains are very large. The values of microstrain seen here are comparable to those recorded in other high-energy environments, such as in ball milled zirconia and yttria-stabilised zirconia powders (Varin *et al.*, 1999; Lin & Duh, 1998).

3.3. Grain Breakdown Mechanism

Considering the data above, we propose the following degradation mechanism responsible for the observed gradual build-up and release of strain within the sample during stress cycling. This mechanism also explains the gradual increase in the peak strain amplitude in consecutive peaks as the damage from successive impacts accumulates. In granular materials with larger domain sizes, dislocation density could explain the oscillations in the microstrain parameter. However, due to the small domain size, the energy required for migration of the dislocations to the grain boundaries (where they are subsequently expelled from the lattice) is considerably lower, allowing for a consistent dislocation density irrespective of shocks (Gleiter, 1989). Consequently, while the dislocation density model could explain an increase in dislocation density after one shock, the energy of the subsequent shot would drive this dislocation out of the lattice. Therefore the dislocation density model does not explain the oscillatory nature of the microstrain parameter, or the subsequent increase in oscillation amplitude.

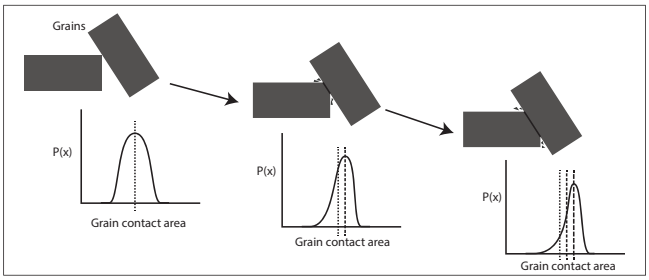

Fig. 9. Schematic showing the proposed grain breakdown mechanism within the sample. The smallest grain contact areas receive the highest percentage of strain, which slowly degrades the grain contact, increasing the grain contact area. The primary strain source is to the left of the cluster of grains shown.

Instead of dislocations, a more likely cause of this is the damage of grain contacts within the material. As figure 9 shows, neighbouring grains within a material share a grain contact area ($A_{contact}$). The strain wave transfers between adjacent grains across

this area. A passing strain wave produces a certain force at the contact. If this force exceeds the strength of the material, the grain will fail locally, producing a larger contact area and a small amount of disordered "debris". This enlarged contact will be able to withstand a strain wave of the same magnitude since the force, F, contained in it has to pass through a larger cross section, $A_{contact}$, resulting in smaller stress, $\varsigma = F/A_{contact}$. Subsequent microstrain amplitude oscillations are observed whenever a larger strain wave passes through the contact, causing further degradation and increase in the contact area. This mechanism has very little effect on the overall column sizes of any particular crystallographic orientation since only small areas at the edges of the grain are removed. This suggests that the smaller $A_{contact}$ is, the higher the strain experienced by the sample at this contact. With each subsequent shot, these small contact areas will exhibit a high amount of strain. This high strain damages the grain contacts; breaking off corners, leaving behind a slightly larger grain contact area. With larger grain contact areas between neighbouring grains, the energy these contacts can retain before breaking increases, thus explaining the gradual increase of peak strain amplitude. Figure 9 also shows schematically the changes to grain contact area distributions within the sample. With the proposed model the distribution of $A_{contact}$ will increase in mean value and the width of the distribution will narrow as each cycle creates larger grain contact areas. This will also introduce an asymmetry to the distribution of grain contact areas within the sample due to the preferential damage to the smaller grain contact areas.

The proposed change in domain size would be very small relative to the size of the grains. Corners would sustain damage first, since these contacts would have the smallest area, thus experiencing the highest strain.

4. Conclusions

We have demonstrated a technique which is capable of detecting dynamic strain propagation on a 1 ms time-scale within a polycrystalline medium while retaining sufficient powder averaging to allow whole-pattern fitting. The propagation velocity of strain is on the order of $10^3 ms^{-1}$. High microstrains concentrated locally during the passing of a strain wave after laser impact have been observed in the range $1.01\% < \varepsilon < 1.46\%$ during shocking. This novel method allows the characterisation of potential thermal barrier materials which are more resistant to thermal cycles involving rapid temperature changes (e.g. such as switching fuel cells on or off, or switching between heat sources in different locations in an industrial melting furnace). Aggravated testing is applied in order to stress the materials beyond normal operating thermal cycles and better understand the mechanisms causing deterioration.

A model is proposed for a grain breakdown mechanism within the sample which explains the increasing strength of the strain waves as the number of shocks increases. Further investigation based on a laser peening process using a Nd:YAG laser are planned. The proposed experiment increases the integrated intensity of the laser shot due to a much shorter pulse length.

Acknowledgements

We would like to thank Claire Murray (Diamond) for assistance with the Topas software and Les Dean, Matthew Gunn and David Lewis (Aberystwyth) for help building the sample environment and Stephen Wade of the Institute of Biological, Environmental and Rural Sciences, Aberystwyth University for scanning electron micrographs of our as-prepared samples. We acknowledge Diamond Light Source for funded facility access. MEJ and RW appreciate the support from the European Union's 7th Framework Programme under contract PIAP-GA-2011-286110-INTERCER2.

References

Balzar, D. (1999). *International Union of Crystallography Monographs on Crystallography*, **10**, 94–126.

Bujalski, W., Dikwal, C. M. & Kendall, K. (2007). *J. Power Sources*, **171**(1), 96–100.

Cheetham, A. K. & Goodwin, A. L. (2014). *Nature materials*, **13**(8), 760–762.

Chou, Y.-s. & Stevenson, J. W. (2002). *Journal of Power Sources*, **112**(2), 376–383.

Coelho, A. A. (2004). *A Computer Programme for Rietveld Analysis*.

Gleiter, H. (1989). *Progress in Materials Science*, **33**(4), 223 – 315.

Hsiao, Y. C. & Selman, J. R. (1997). *Solid State Ionics*, **98**(1), 33–38.

Ivers-Tiffée, E., Weber, A. & Herbstritt, D. (2001). *Journal of the European Ceramic Society*, **21**(10), 1805–1811.

Le Bail, A. (2005). *Powder Diffraction*, **20**, 316–326.

Le Messurier, D., Winter, R. & Martin, C. M. (2006). *J. Appl. Crystallogr.* **39**(4), 589–594.

Lee, S., Cavalieri, A., Fritz, D., Swan, M., Hegde, R., Reason, M., Goldman, R. & Reis, D. (2005). *Phys. Rev. Lett.* **95**(24), 246104.

Lin, J.-D. & Duh, J.-G. (1998). *Journal of the American Ceramic Society*, **81**(4), 853–860.

Matus, Y., Dejonghe, L., Jacobson, C. & Visco, S. (2005). *Solid State Ionics*, **176**(5-6), 443–449.

Musgrave, M. (1970). *Crystal acoustics: Introduction to the study of elastic waves and vibrations in crystals*.

Pouchon, M., Degueldre, C. & Tissot, P. (1998). *Thermochimica acta*, **323**(1), 109–121.

Prabhu, G. & Bourell, D. (1995). *Nanostructured Mater.* **6**(21), 361–364.

Reis, D., DeCamp, M., Bucksbaum, P., Clarke, R., Dufresne, E., Hertlein, M., Merlin, R., Falcone, R., Kapteyn, H., Murnane, M., Larsson, J., Missalla, T. & Wark, J. (2001). *Phys. Rev. Lett.* **86**(14), 3072–3075.

Ronchi, C. & Sheindlin, M. (2002). *International journal of thermophysics*, **23**(1), 293–305.

Rose-Petruck, C., Jimenez, R., Guo, T., Squier, J. A., Walker, B. C. & Wilson, K. R. (1999). **398**, 310–312.

Salamatov, E. I. (2007). *physica status solidi (b)*, **244**(6), 1895–1899.

Steele, B. C. & Heinzel, A. (2001). *Nature*, **414**(6861), 345–52.

Teixeira, V., Andritschky, M., Fischer, W., Buchkremer, H. P. & Sto, D. (1999). *Surf. Coatings Technol.* **121**, 103–111.

Theunissen, G., Winnubst, A. & Burggraaf, A. (1989). *Mater. Sci. Lett.* **8**, 55–57.

Thompson, S. P., Parker, J. E., Marchal, J., Potter, J., Birt, A., Yuan, F., Fearn, R. D., Lennie, A. R., Street, S. R. & Tang, C. C. (2011). *Journal of synchrotron radiation*, **18**(4), 637–648.

Thompson, S. P., Parker, J. E., Potter, J., Hill, T. P., Birt, A., Cobb, T. M., Yuan, F. & Tang, C. C. (2009). *Rev. Sci. Instrum.* **80**(7), 075107.

Varin, R., Bystrzycki, J. & Calka, A. (1999). *Intermetallics*, **7**(8), 917–930.

Synopsis

Dynamic strain propagation in granular ceramics presents a cause of failure in industrial materials that undergo rapid thermal cycling. Using synchrotron X-ray powder diffraction after successive laser impacts it is shown that rapid stress cycles induce large strains which propagate throughout the bulk, and strain build-up and subsequent release is seen in the sample. A mechanism based on degradation of grain contacts is proposed to explain the oscillatory nature of microstrain.